234 (2024) 212586

Contents lists available at ScienceDirect

Geoenergy Science and Engineering

journal homepage: www.sciencedirect.com/journal/geoenergy-science-and-engineering

Permeability enhancement by CO_2 injection and chelating agent stimulation for creating geothermal reservoirs in granite

Eko Pramudyo [a,*], Luis Salalá [a,b], Ryota Goto [c], Jiajie Wang [a], Kazumasa Sueyoshi [a], Lena Muhl [d,e], Kiyotoshi Sakaguchi [a], Noriaki Watanabe [a,**]

[a] Department of Environmental Studies for Advanced Society, Graduate School of Environmental Studies, Tohoku University, Sendai, 9808579, Japan
[b] Department of Mechanical Engineering, Faculty of Engineering and Architecture, University of El Salvador, San Salvador, El Salvador
[c] Taisei Advanced Center of Technology, Taisei Corporation, Yokohama, 2450051, Japan
[d] Department of Geothermal Science and Technology, Institute of Applied Geosciences, Technical University of Darmstadt, Schnittspahnstraße 9, 64287, Darmstadt, Germany
[e] GFZ German Research Centre for Geosciences, Section 4.8: Geoenergy, Telegrafenberg, 14473, Potsdam, Germany

ARTICLE INFO

Keywords:
CO_2 fracturing
Chelating agent injection
Permeability enhancement
Differential stress
Geothermal reservoir

ABSTRACT

Existing research indicates that to create geothermal reservoirs using CO_2 injection, additional stimulation methods are necessary. *N, N*-bis(carboxymethyl)-L-glutamic acid (GLDA) injection has been predicted to increase the permeability of CO_2 injection-induced cloud-fracture networks (CFNs) and could serve as an additional stimulation method. Nevertheless, the influence of differential stress, flow geometry, and scale on the characteristics of permeability enhancement by GLDA injection is yet to be clarified. Accordingly, this study experimentally elucidated the permeability enhancement characteristics of injecting a chelating agent in fractured granite under differential stress conditions as an additional method for creating geothermal reservoirs using CO_2 injection. GLDA injection experiments were conducted on fractured-granite samples under conventional- and true-triaxial stress states under varying differential stress and pH conditions. Regardless of the differential stress and pH conditions, rock deformation and acoustic emission (AE) were negligible during the chelating agent flow-through experiments on the fractured samples, whereas similar permeability enhancement factors were achieved within the same duration. Thus, stress did not affect the permeability enhancement by chelating agent injections. The permeability enhancement factors were inferred to be high near the injection borehole because of the high viscosity of the solution. Therefore, reservoir stimulation should be conducted using low-concentration chelating agent solutions at constant injection pressures. The study provides insights into the stimulation strategies for creating geothermal reservoirs using CO_2 injection.

1. Introduction

Hydraulic stimulation to induce shear dilation of natural fractures (hydroshearing) or to develop new fractures (i.e., induced fractures) is the primary method for increasing rock permeability to create enhanced geothermal system (EGS) reservoirs (Tester et al., 2006). At superhot geothermal conditions (>~400 °C), formation of complex cloud-fracture networks (CFNs), a network of permeable microfractures densely distributed over rock body, has been experimentally demonstrated in granite (Watanabe et al., 2017b; 2019). Accordingly, CFNs form through stimulation of pre-existing microfractures by the injected low-viscosity (<100 μPa·s) water near and above its critical temperatures. Thus, Goto et al. (2021) showed that Griffith failure criterion can be used to predict the pore pressure at which CFN forms (fracture-formation pressure). Compared to simple, bi-winged hydraulic fractures induced by cold water injection, CFNs potentially facilitate a more effective heat extraction from geothermal reservoirs. This is because complex fracture network provides a larger total heat-exchange surface and creates longer, indirect fluid paths between injection and production wells, preventing cold injected fluid to flow quickly to the production wells (Yu et al., 2021; Cao and Sharma, 2023).

Nevertheless, water utilization is characterized by specific challenges, such as difficulties in maintaining the permeability in a water-

* Corresponding author.
** Corresponding author.
E-mail addresses: eko.pramudyo.c3@tohoku.ac.jp (E. Pramudyo), noriaki.watanabe.e6@tohoku.ac.jp (N. Watanabe).

https://doi.org/10.1016/j.geoen.2023.212586
Received 6 October 2023; Received in revised form 17 November 2023; Accepted 10 December 2023
Available online 14 December 2023

Abbreviations

EGS	enhanced geothermal system
CFN	cloud-fracture network
GLDA *N*,	*N*-bis(carboxymethyl)-L-glutamic acid
CT	computed tomography
AE	acoustic emission
PE	polyethylene
ICP-OES	inductively coupled plasma optical emission spectrometry
arb unit	arbitrary unit

based superhot EGS owing to the competition between free-face dissolution and the stress solution of fracture asperities (Watanabe et al., 2020), and concerns over fracture clogging by amorphous silica formed during phase changes in granite-reacted water from subcritical to supercritical or superheated steam in granite (Watanabe et al., 2021a).

Therefore, CO_2 has been proposed as an alternative fracturing fluid in EGS applications (Ishida et al., 2016; Isaka et al., 2019), because it is less reactive to the rock-forming minerals (Brown, 2000; Pruess, 2006), can reduce water footprint (Wilkins et al., 2016), and has low viscosity (<100 μPa·s) at 150–500 °C and 10–100 MPa (Heidaryan et al., 2011), allowing for CFN formation in conventional (c.a. 150–300 °C) and superhot geothermal conditions. Additionally, CO_2 is safer and easier to handle than the competing alternatives of N_2 and He, and does not require special equipment during fracturing operations, such as low-temperature storage when N_2 is used (Gandossi and Estorff, 2015; Moridis, 2018). CO_2 is also denser than N_2 and He; hence, it is easier to achieve the intended pressure at greater depths (Gandossi and Estorff, 2015; Moridis, 2018).

Pramudyo et al. (2021) experimentally demonstrated that CO_2 injection can induce CFNs in granite under conventional and superhot geothermal conditions. The CFNs were formed through the same mechanism as those occurring under superhot conditions; thus, the Griffith failure criterion also applies to both geothermal conditions. CO_2 injection was also shown to induce large shear displacements on pre-existing fractures and CFN in the (unfractured) rock matrix (Pramudyo et al., 2023), both of which would benefit reservoir creation in naturally fractured geothermal environments (i.e., geothermal environments with meter-scale natural fractures, as implied by Tester et al., 2006). Nonetheless, studies (Pramudyo et al., 2021; 2023) have also revealed that CO_2 injection-induced CFNs formed under conventional geothermal conditions and small differential stress ($\sigma_1-\sigma_3$; where σ_1 is the maximum principal stress, MPa, σ_3 is the minimum principal stress, MPa), and those in rocks with pre-existing fractures comprised narrow fractures (implying low-permeability enhancement). Therefore, additional stimulation methods are necessary to create geothermal reservoirs using CO_2 injection.

Long-duration pressurization at or higher than fracture formation pressure enhances fluid flow into pre-existing microfractures and promotes fracturing in the unfractured zone (i.e., flow-induced microfracturing), as well as increases the fracture aperture in CFNs (Goto et al., 2021). Nonetheless, there is concern regarding the increased risk of large-magnitude induced seismicity with high-pressure injections in the presence of faults (Kwiatek et al., 2019; Rutqvist and Rinaldi, 2019), especially under conventional geothermal conditions, where rocks have higher elasticities than those under superhot geothermal conditions (e.g., Gautam et al., 2018). Therefore, hydraulic stimulation under conventional geothermal conditions should be employed in conjunction with chemical stimulation to achieve adequate permeability enhancement.Watanabe et al. (2021b) and Takahashi et al. (2023) have proposed the use of an eco-friendly chelating agent, *N, N*-bis (carboxymethyl)-L-glutamic acid (GLDA), to selectively dissolve rock-forming minerals and enhance rock permeability.

Permeability enhancement in fractured granite samples by injecting GLDA-containing aqueous (aq.) solution with varying pH was demonstrated at 200 °C and confining stress conditions ($\sigma_1 = \sigma_2 = \sigma_3$; where σ_2 is the intermediate principal stress, MPa) (Watanabe et al., 2021b; Takahashi et al., 2023). Accordingly, permeability enhancement under acidic conditions occurs by creating voids induced by the selective dissolution of biotite and the formation of preferential flow paths (i.e., fracture widening) connecting the voids. The permeability enhancement under alkaline conditions was caused by an increase in the fracture aperture induced by the enhanced dissolution of quartz (comprising approximately 30% of the granite samples). The largest permeability enhancement factor (i.e., the resulting permeability divided by the initial permeability) was achieved by GLDA injection at pH 4, when a single-pH solution was used. Moreover, the optimum permeability enhancement factor was achieved by successive injections of GLDA at pH 4 and 8 (Watanabe et al., 2021b; Takahashi et al., 2023).

Therefore, GLDA injection was predicted to increase the permeability of CO_2 injection-induced CFNs and could serve as an additional stimulation method. Nevertheless, the influence of differential stress, at which the CFNs form and have the potential to deform, on the characteristics of permeability enhancement by GLDA injection is yet to be elucidated. Mineral dissolution may or may not promote fracture deformation. Moreover, permeability enhancement in a fracture network under large-scale and radial flow conditions must be elucidated.

Thus, this study aimed to elucidate the characteristics of permeability enhancement by GLDA solution injection in CO_2 injection-induced CFNs, considering the influence of stress states, scale, and flow geometry. Accordingly, GLDA injection experiments were conducted on fractured-granite samples at 200 °C under conventional- and true-triaxial stress states under varying differential stress and pH conditions. The findings will provide insights into the preferable stimulation strategies for creating geothermal reservoirs using CO_2 injection and additional stimulation methods.

2. Methods

2.1. Experiments under conventional-triaxial stress states

Experiments under conventional-triaxial stress ($\sigma_1 > \sigma_2 = \sigma_3$) were performed on cylindrical Inada granite samples (diameter, 30 mm; length, 25 mm) with a single borehole (diameter, 1.5 mm; length, 10 mm) (Fig. 1a). The sample small size allowed the identification of the effect of stress state and pH variation on permeability enhancement by CO_2 fracturing and chelating agent injection, without strong influence of scale (e.g., permeability enhancement variation due to distance from injection point). The tensile and compressive strengths, Young's modulus, porosity, and intrinsic permeability of the granite near atmospheric temperature and pressure are 4–9 MPa, 160–180 MPa, 55–80 GPa, 0.5−0.8%, and 2–8 × 10^{-18} m^2, respectively (Watanabe et al., 2017a; Goto et al., 2021; Yamaguchi, 1970; Lin et al., 2003). Inada granite, by volume, comprises 33.7% quartz (ideal chemical formula: SiO_2), 32.1% K-feldspar (ideal chemical formula: $KAlSi_3O_8$), 30.3% plagioclase-feldspars (chemical formula for each end-member: $NaAlSi_3O_8$ and $CaAl_2Si_2O_8$), 3.8% biotite (ideal chemical formula: $K(Mg,Fe)_3AlSi_3O_{10}(OH,F)_2$), and 0.1% other minerals (Ishihara, 1991; Sasada, 1991; Takahashi et al., 2011; Takaya, 2011).

The experiments comprised CO_2 fracturing and chelating-agent flow-through experiments on the fractured samples (Fig. 2a). X-ray computed tomography (CT) was performed on the samples before and after CO_2 fracturing, as well as after the chelating-agent flow-through experiments. X-ray CT was conducted at c.a. 23 °C and atmospheric pressure conditions, at an X-ray tube voltage of 120 kV, tube current of 150 μA, and voxel size of 16.6 μm to verify CFN formation and the subsequent mineral dissolutions. Additionally, the porosity of the samples post-

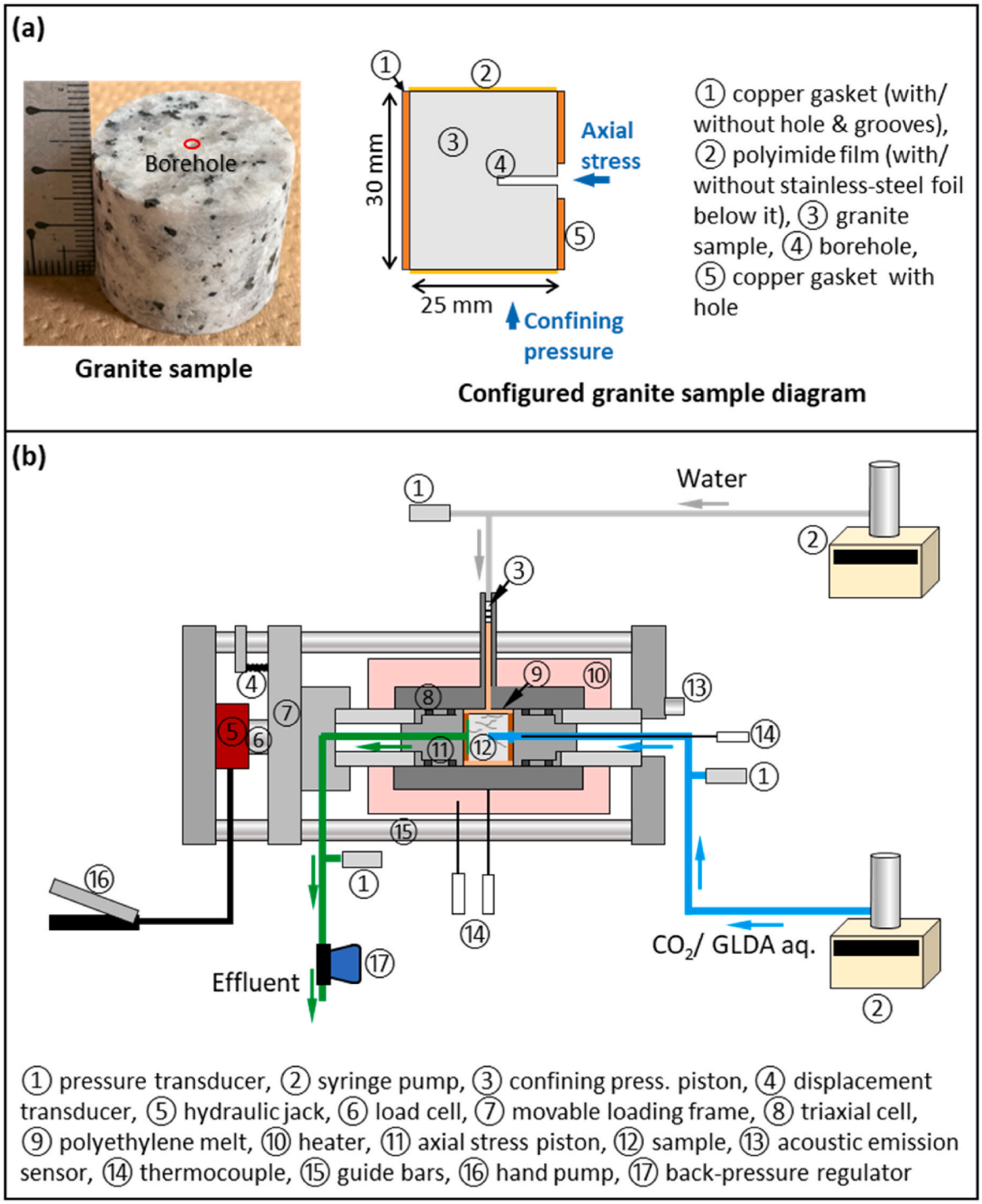

Fig. 1. (a) Example of a cylindrical granite sample, diagram of the configured sample, and the loading condition. (b) Design for the CO_2 fracturing and chelating agent flow-through experiments under conventional triaxial stress conditions.

experimentation was estimated from the X-ray CT data using Molcer Plus 3D image visualization and processing software (White Rabbit Corporation, Tokyo, Japan) to provide insights into the degree of void formation in the experiments. Porosity was defined as the sum volume of voids larger than 27 voxels (i.e., distinguishable voids) divided by the bulk volume of the rock.

Chelating agent solutions were prepared from a 40 wt% aqueous GLDA-Na_4 ($C_9H_9Na_4O_8$) solution purchased from Tokyo Chemical Industry Co. Ltd. The molar concentration of GLDA-Na_4 in the initial solution has been calculated as approximately 1.3 mol·L^{-1} (Wang et al., 2022). Dilutions were performed to make 20 wt% GLDA-Na_4 solutions, and the pH was adjusted to 4 or 8 by adding nitric acid. At 5 MPa and 200 °C, the GLDA solution viscosities at pH 4 and 8 were 304.2 and 286.6 μPa·s, respectively. The high viscosities implied that GLDA solution penetration and mineral dissolution would occur effectively only in certain wider fractures within the CFNs. Thus, under differential stress conditions, significant rock deformation may not be promoted, even at considerable pore pressures. Significant deformations are likely to occur during the injection of low-viscosity CO_2.

The experiments were performed using a conventional triaxial stress

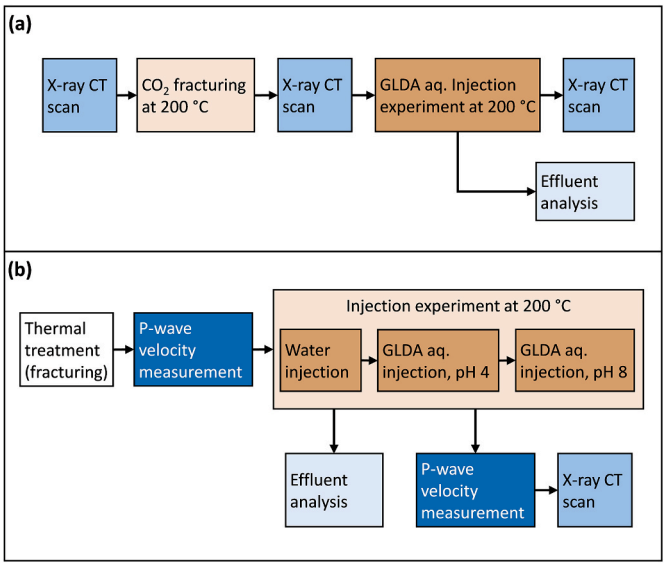

Fig. 2. Workflow for (a) experiments under conventional-triaxial stress states ($\sigma_1 > \sigma_2 = \sigma_3$), and (b) experiment under true-triaxial stress state ($\sigma_1 > \sigma_2 > \sigma_3$).

experimental and acoustic emission (AE) measurement system (Fig. 1b), as described by Watanabe et al. (2017a, 2017b) and Goto et al. (2021). Primarily, the system comprised a triaxial cell that employed molten plastic (e.g., polyethylene – PE, for experimentation at 120–300 °C) as confining pressure fluid, two cylindrical axial stress pistons equipped with a centered fluid flow-path and pipe, a linear variable differential transformer to measure axial deformation of the sample, syringe pumps for fluid injection, and AE measurement system to monitor AE energy during the experiment. For the AE measurement system, Physical Acoustics Corporation's two-channel data acquisition and digital signal processing PCI-2 with an R15α 150-kHz resonant frequency sensor were used. Here, the AE energy was calculated as the time integral of the amplitude (voltage) and presented in arbitrary units (arb units) after the background noise was eliminated. The injected fluid was heated to the experimental temperature before it reached the sample, as confirmed using a thermocouple inside the injection pipe (Fig. 1b).

The sample and experimental system for CO_2 fracturing were configured to be the same as those in Pramudyo et al. (2021). The sample was sleeved by a 50-μm thick polyimide film, where copper gaskets were placed at the end faces of the sample. The gasket on the sample injection side had a central hole to allow fluid injection into the sample borehole. For the chelating-agent flow-through experiment, the fractured sample was sleeved using stainless-steel foil (10-μm thick) and polyimide film. Copper gaskets with centered holes were placed on the sample end faces, and the gasket on the production side contained concentric and radial grooves to channel the produced fluid to the production pipe. In both CO_2 fracturing and chelating agent flow-through experiments, the sleeved sample was placed in a PE cylinder inside the triaxial cell and subsequently heated to the experimental temperature. The axial stress (corresponding to σ_1) and confining pressure (corresponding to σ_2 and σ_3) were increased to the intended stress state once the sample reached the experimental temperature.

To elucidate the permeability enhancement process by CO_2 fracturing and the injection of a weakly acidic (pH 4) chelating agent under varying differential stress, two experimental runs (Runs 1 and 2) were performed at 200 °C (Table 1). In Run 1, CO_2 fracturing was first performed at axial stress and confining pressure of 70 and 30 MPa, respectively (i.e., differential stress, = 40 MPa). Subsequently, under the same stress state, a chelating agent flow-through experiment was performed. In Run 2, CO_2 fracturing and subsequent flow-through experiments were performed at axial stress and confining pressure of 100 and 30 MPa, respectively (i.e., differential stress = 70 MPa). Furthermore, to understand permeability enhancement by CO_2 fracturing and injection of a weakly alkaline (pH 8) chelating agent under a differential stress condition, another experimental run (Run 3) was performed at 200 °C and axial stress and differential pressure of 100 and 30 MPa, respectively (i.e., differential stress = 70 MPa).

Table 1
Conditions for CO_2 fracturing and chelating agent flow-through experiments.

	Experiment type	pH of aq. GLDA	Temp. (°C)	Stress state			
				σ_1	σ_2	σ_3	$\sigma_1-\sigma_3$
Run 1	CO_2 fracturing, followed by GLDA injection	4	200	70	30	30	40
Run 2	CO_2 fracturing, followed by GLDA injection	4	200	100	30	30	70
Run 3	CO_2 fracturing, followed by GLDA injection	8	200	100	30	30	70
Run 4	GLDA injection on thermally-fractured sample	4, followed by 8	200	45	20	10	35

During the experiments, CO_2 was injected at a rate of 1 mL·min^{-1} from room temperature (c.a. 10–20 °C) and an initial borehole pressure of 10 MPa, using a syringe pump. CO_2 injection-induced CFNs form at fracture formation pressures ($P_{p,frac}$, MPa) predictable by Griffith failure criterion (Pramudyo et al., 2021). Accordingly, $P_{p,frac}$ is given as follows (Griffith, 1924; Jaeger et al., 2007; Secor, 1965; Cox, 2010):

$$P_{p,frac} = \frac{8\sigma_t(\sigma_1+\sigma_3)-(\sigma_1-\sigma_3)^2}{16\sigma_t} \; at \; (\sigma_1-\sigma_3) \geq 4\sigma_t, \quad (1)$$

$$P_{p,frac} = \sigma_3 + \sigma_t \; at \; (\sigma_1-\sigma_3) < 4\sigma_t, \quad (2)$$

where σ_t is the rock tensile strength (MPa). Assuming borehole pressure equals to pore pressure due to CO_2 infiltration into pre-existing microfractures, CFNs in the experiments were expected to form at borehole pressure of 35.7 MPa for Run 1, and 21.25 MPa for Run 2 and 3 [Eqs. (1) and (2)]. To increase the CFN visibility in the post-CO_2 fracturing X-ray CT measurement based on the flow-induced microfracturing process (Goto et al., 2021), the CO_2 injection pressure was increased to 45 MPa in Run 1 and 30 MPa in Runs 2 and 3, which were higher than the expected values of fracture formation pressure.

In the chelating agent flow-through experiments, the GLDA solution was first injected from both injection and production sides at a constant pressure of 26 MPa for approximately 20 min to saturate the sample with the GLDA solution. This procedure was performed to avoid evaporation of the solution and deposition of GLDA in the fractures, which would otherwise have occurred if the solution had been injected from one side. The injection and production pressures were then set to 28 and 26 MPa, respectively, and maintained constant for 5 h, during which the GLDA solution flowed through the sample. The injection and production pressures were close to the confining pressure to optimize the penetration of the GLDA solution into the CFN. Nonetheless, these pressures were lower than the maximum injection pressure values during CO_2 fracturing to prevent fracture propagation owing to the increase in pore pressure.

The permeability values of the sample were not obtained during these experiments because the flow geometry in the sample would have been a combination of the first radial flow from the borehole and then the flow towards the production surface of the sample. The combined flow geometries made the permeability computations too complex to meet the objective of the experiments. Nonetheless, the permeability changes in the sample could be assessed by changes in the injection flow rates, computed at a 5-min interval, based on Darcy's law. Accordingly, injection rate is a reasonable proxy of hydraulic resistance under constant injection and production pressure, assuming injection rate equals

to flow rate in the small-scale sample. Thus, the permeability enhancement factor can also be defined as the ratio of the injection flow rate at a time to the initial injection flow rate. All effluents from each experiment were collected for analyzing the concentrations of elements (Al, Ca, Fe, K, Mg, and Si) eluted from the minerals, using inductively coupled plasma optical emission spectrometry (ICP-OES).

2.2. Experimentation under true-triaxial stress state

An experiment under a true-triaxial stress state (Run 4, Table 1) was performed to elucidate the permeability enhancement process by GLDA solution injection on a large scale and under radial flow geometry. The experiment was performed on a 100 × 100 × 100 mm Inada granite cube (Fig. 3a), which had been thermally treated at 500 °C and atmospheric pressure for 10 h to induce a dense network of microfractures (Fig. 2b). The thermally induced network of microfractures is analogous to a CFN (Goto et al., 2023). The sample had chamfered edges to accommodate rock deformation during the experiment. The sample also contained a centered borehole (diameter = 10 mm) connecting two opposite faces of the sample.

P-wave velocity measurements were performed on the sample before and after the experiment at room temperature (c.a. 10–20 °C) and atmospheric pressure conditions to determine the distribution of voids and wide fractures post-experimentation. For the measurement, each sample face was divided into 3 × 3 pixels, and the travel time between each opposing pair at a distance of 100 mm was measured to compute the 27 P-wave velocities. The measurements provided the distribution of P-wave velocities within the sample, and the velocities at each voxel were estimated to assess the fracture pattern by solving a system of 27 equations in the following form:

$$\frac{1}{V_p} = \frac{\frac{1}{V_{p1}} + \frac{1}{V_{p2}} + \frac{1}{V_{p3}}}{3}, \tag{3}$$

where V_p is the velocity ($m{\cdot}s^{-1}$) for each pixel pair, and V_{p1}, V_{p2}, and V_{p3} are the respective velocities ($m{\cdot}s^{-1}$) for voxels between pairs.

The experiments were performed using the true triaxial stress experimental system described by Watanabe et al. (2019) and Goto et al. (2021). In the system, the sample was placed inside a triaxial cell so as the borehole was vertical (parallel to Z axis; Fig. 3b and c). Three principal stresses were induced in the sample using six cylindrical pistons with square loading faces that corresponded to the sample square-loading faces (Fig. 3b). Each piston contains cartridge heaters and a fluid flow path connected to a pressure transducer (Fig. 3c). The rooms between the chamfered edges of the sample and chamfered faces of the pistons were filled with pressurized molten PE during the experiment. Two pistons with a centered fluid flow path were positioned at the top and bottom of the sample and provided the maximum principal stress (σ_1) in vertical direction via stainless-steel gaskets containing a centered hole with a rubber O-ring. The fluid flow path in the bottom piston was connected to a syringe pump for fluid injection into the sample borehole, and the flow path in the top piston was connected to a closed pipe. The thermocouple in the top flow path was extended to measure the temperature at the center of the sample. Copper gaskets with radial and concentric grooves were placed on the side faces of the sample to direct produced fluid into the flow path of the horizontal pistons. An AE sensor (from the same AE measurement system described in Section 2.1) was placed into the elastic-wave guide bar located on the opposite side of the loading side of the piston in the σ_2-direction (parallel to X axis).

Fluid was injected at 200 °C, σ_1 = 45 MPa, σ_2 = 20 MPa, σ_3 = 10 MPa, and production pressure (pressure at sample side faces) = 2 MPa. The stress values represented an approximately 1.8 km deep geothermal environment in normal-faulting regime, assuming rock density of 2.6 $gr{\cdot}cm^{-3}$. Initially, water was injected into the borehole at 1 $mL{\cdot}min^{-1}$ to determine AE energy level and deformation rates under negligible chemical reaction condition in the sample (i.e., background condition). At pH 4, GLDA solution was then injected for 2 h, followed by injection at pH 8 for another 2 h, both at a flow rate of 1 $mL{\cdot}min^{-1}$. This strategy was employed to demonstrate the optimum permeability enhancement (Takahashi et al., 2023) on a large-scale rock. The GLDA solution was assumed to flow in the radial direction from the centered borehole in the sample. Therefore, the permeability changes in the sample can be estimated using the following equation (adapted from Dake (1983)):

$$P_b - P_s = \frac{q\mu}{2\pi hk} ln\frac{r_s}{r_b}, \tag{4}$$

$$P_b - P_s = \frac{q\mu}{2\pi hk_1} ln\frac{r_1}{r_b} + \frac{q\mu}{2\pi hk_2} ln\frac{r_s}{r_1}, \tag{5}$$

where P_b is the borehole pressure (Pa), P_s is the production pressure (Pa), q is the flow rate ($m^3{\cdot}s^{-1}$), μ is the dynamic viscosity of fluid (Pa·s), r_b is the borehole radius (m), r_s is the sample radius (in this case, distance from the center to the side face of the sample, expressed in meters), h is the borehole length (m), k is the sample average permeability (m^2), k_1 is the permeability (m^2) of the zone near the borehole within the radius r_1 (m), and k_2 is the permeability (m^2) of the zone between r_1 and r_s. Based on Eqs. (4) and (5), the enhancement in the average permeability of the sample is reflected by a decrease in the differential pressure when a constant flow rate is used.

The effluent was collected once during the water injection and then at 10-min interval from the start of the GLDA injection to be later analyzed using ICP-OES. The analysis provided insights into the evolution of the Al, Ca, Fe, K, Mg, and Si concentrations in the effluent, thus, clarifying the mineral dissolution process in the sample. X-ray CT imaging was performed on the cores (length: 50 mm, diameter: 25 mm) obtained from the sample post-experimentation to verify the distribution of mineral dissolution with respect to the distance from the borehole. Three cores were obtained parallel to the borehole (i.e., σ_1 direction) from around the borehole and near the sample side faces at the centered $\sigma_1 - \sigma_2$ and $\sigma_1 - \sigma_3$ planes. X-ray CT scans were performed under atmospheric conditions at an X-ray tube voltage of 120 kV, tube current of 150 μA, and voxel size of 10 μm. Porosity estimation using the Molcer Plus software was also performed based on the X-ray CT data to provide additional insights into the degree of mineral dissolution around the borehole versus near the sample side faces.

3. Results and discussion

3.1. Influence of differential stress on permeability enhancement

Figs. 4–6 show borehole pressure, AE energy, and X-ray CT sections from CO_2 fracturing in Runs 1, 2, and 3. The results were consistent with those reported by Pramudyo et al. (2021). An increase in the AE activity and cumulative AE energy occurred at a borehole pressure of 29 MPa (i.e., $P_{p,frac}$), indicating CFN formation in Run 1. CFN formation occurred at 25 and 27 MPa in Runs 2 and 3, respectively. The $P_{p,frac}$ values were close to those predicted by the Griffith failure criterion for σ_t = 7 MPa. The X-ray CT sections revealed CFN with fractures distributed rather evenly in the samples. Based on the number of visible fractures in the X-ray CT sections, the fractures formed in Run 1 were narrower than those in Runs 2 and 3, with larger differential stress. Moreover, the fractures formed in Run 3 were narrower than those formed in Run 2, with the same differential stress. This difference was likely due to the variation in Young's modulus and tensile strength among the samples, as implied by previous experimental results (Pramudyo et al., 2021).

Fig. 7 shows the fluid pressures and injection flow rate of the GLDA solution in Run 1. Relatively small but continuous axial shortening (in the order of 10^{-2} $\mu m{\cdot}min^{-1}$), along with sparse and low-energy (c.a. 10 arb units) AE activity occurred since the beginning of this experiment. Similar phenomena were observed in the GLDA-flow through experiments of Runs 2 and 3. In contrast, CFN formation generally produces

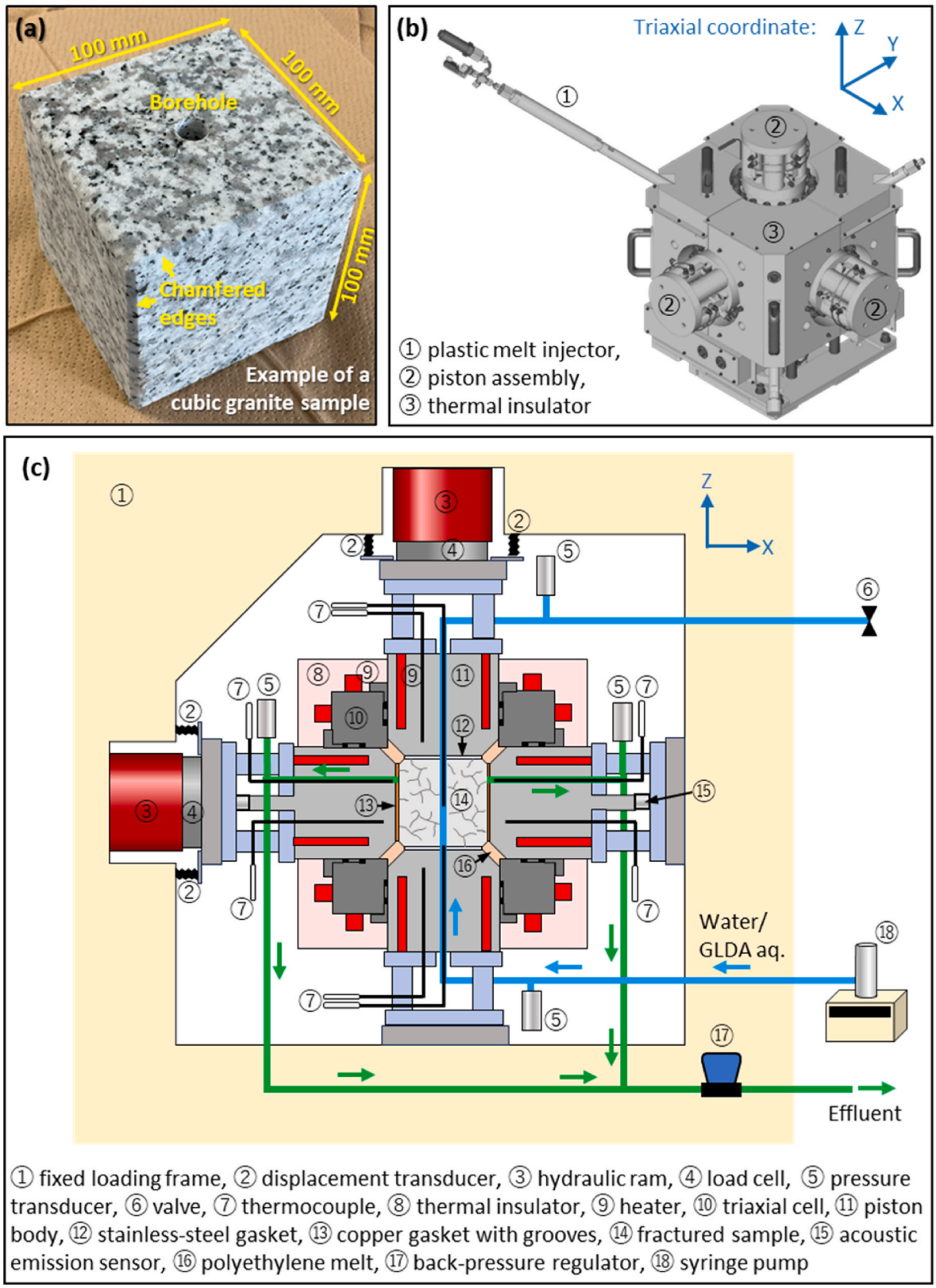

Fig. 3. (a) Example of a cubic granite sample, (b) high-temperature true-triaxial cell, and (c) design of the chelating agent flow-through experiment under true-triaxial stress condition.

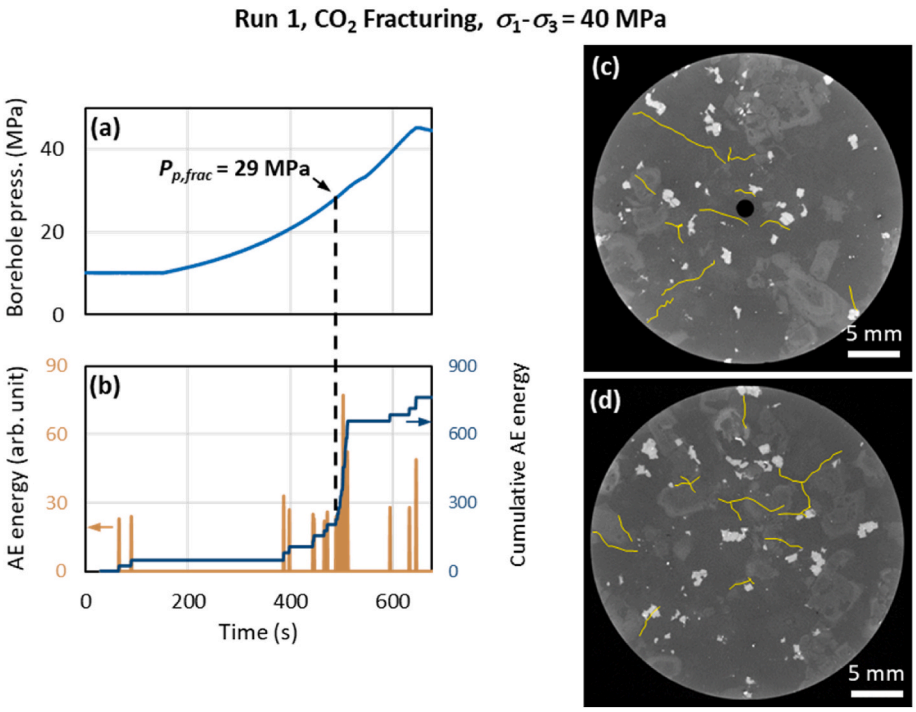

Fig. 4. Results of CO_2 fracturing in Run 1: (a) borehole pressure, (b) AE energy (brown) and cumulative AE energy (blue), X-ray CT section of the sample (c) around borehole and (d) beyond borehole. Fractures are highlighted in yellow to increase grayscale visibility.

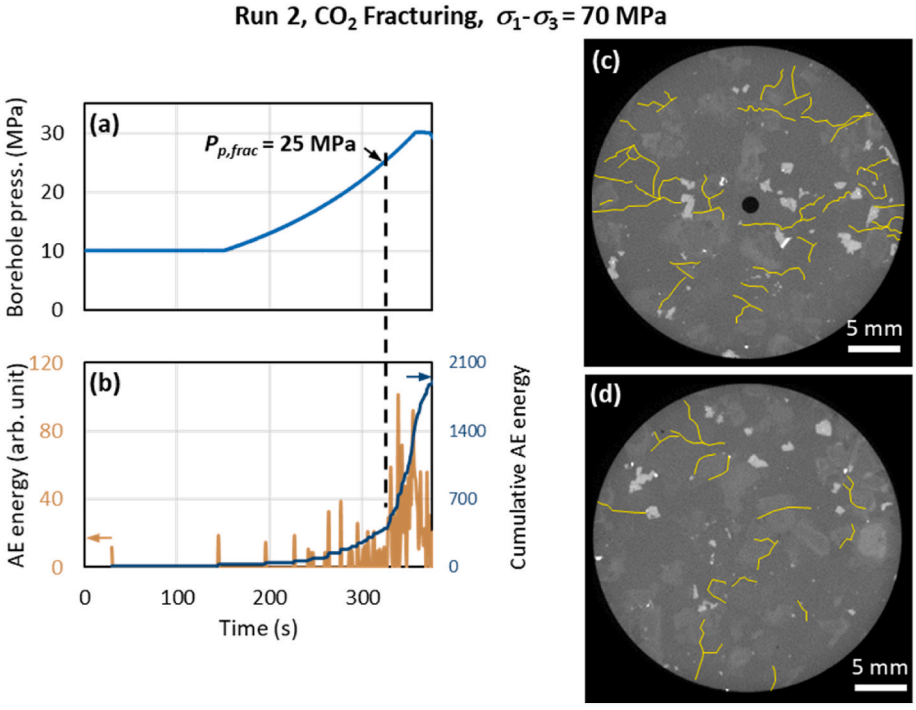

Fig. 5. Results of CO_2 fracturing in Run 2: (a) borehole pressure, (b) AE energy (brown) and cumulative AE energy (blue), and X-ray CT section of the sample (c) around borehole and (d) beyond borehole. Fractures are highlighted in yellow to increase grayscale visibility.

axial deformation in the order of $10^{-1} - 10^{0}$ μm·min^{-1}, and continuous AE activity with energy of >30 arb unit. Therefore, the axial deformation and corresponding AE activity were considered negligible in the GLDA flow throughout the experiments. Owing to the high viscosities (c. a. 300 μPa·s), the GLDA solutions might effectively penetrated only certain number of wider fractures in the CFNs, or penetrated the CFNs in limited locations. Thus, the pressure, void formation, and fracture widening, owing to mineral dissolution, did not cause significant changes in the effective stresses within the rock or significant rock deformation. Significant rock deformation would potentially occur if CO_2 (viscosity of c.a. 24 μPa·s) was injected at the same pressure values, via CO_2 penetration into most fractures in the CFNs. Nevertheless, mineral dissolution continuously increased the sample permeability throughout the experiments. In Run 1, a permeability enhancement

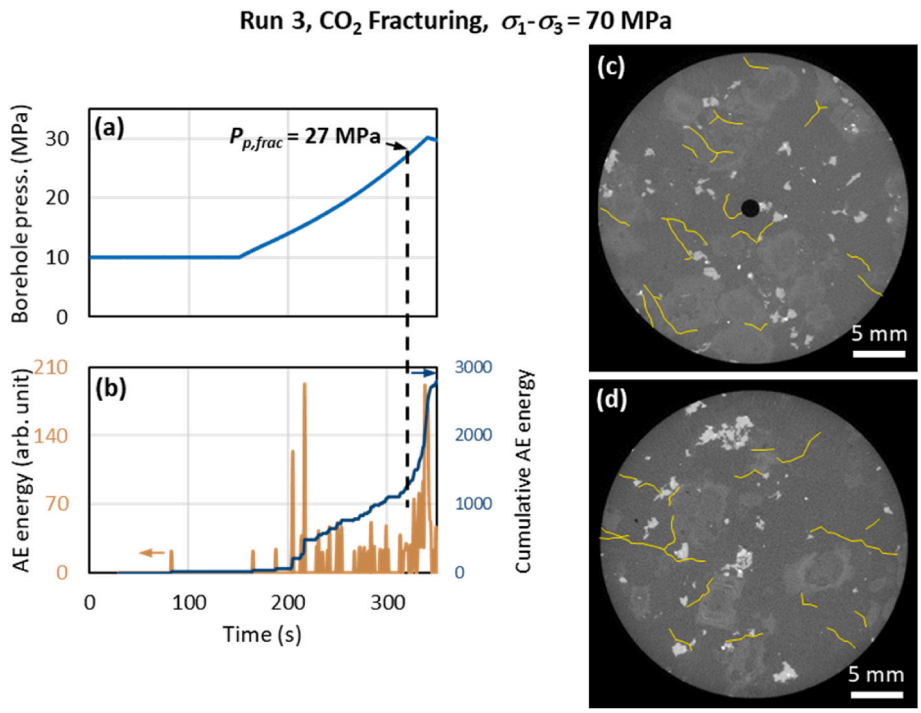

Fig. 6. Results of CO_2 fracturing in Run 3: (a) borehole pressure, (b) AE energy (brown) and cumulative AE energy (blue), and X-ray CT section of the sample (c) around borehole and (d) beyond borehole. Fractures are highlighted in yellow to increase grayscale visibility.

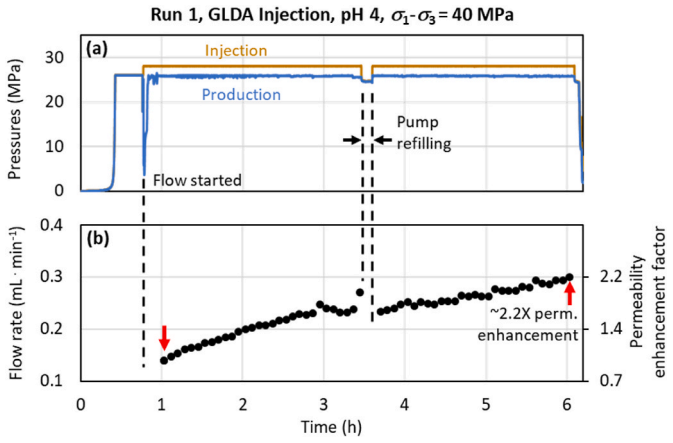

Fig. 7. (a) Injection and production pressures, and (b) calculated injection flow-rates and the corresponding permeability enhancement factor during GLDA flow-through in Run 1. Final permeability enhancement factor was obtained based on the two flow rate values pointed by red arrows.

factor of approximately 2.2 was achieved in 5 h based on the comparison of the two flow-rate values indicated by the red arrows in Fig. 7b.

Permeability enhancement was attributed to fracture widening and void formation owing to biotite dissolution, as observed in the X-ray CT sections of the sample post-experimentation (Fig. 8a). Although not evident, the number of voids appeared to be higher near the boreholes. The estimated porosity of the samples post-experimentation was approximately 0.064%, which was lower than the known porosity values (about 0.5–0.8%) of intact Inada granite. This is because porosity was estimated using X-ray CT data in this study. The elevated Fe concentration in the effluent (Fig. 9) indicated biotite dissolution, and the Si, Al, and Ca concentrations in the effluent indicated the dissolution of feldspar minerals, which was in turn responsible for the observed fracture widening. These results were consistent with those of previous studies on the injection of GLDA solution into Inada granite under the same temperature and pH conditions (Watanabe et al., 2021b; Takahashi et al., 2023).

In experimental Run 2, continuous permeability enhancement resulted in an enhancement factor of c.a. 2.4 within 5 h (similar to that in Run 1) (Fig. 10) with a larger differential stress. X-ray CT images post-experimental Run 2 (Fig. 8b) also suggested a qualitatively similar degree of void formation and fracture widening (porosity of approximately 0.097%) to those observed in Run 1. Moreover, each element analyzed in the effluent from Run 2 was at a concentration similar to that in the effluent from Run 1 (Fig. 9).

The fluid pressures and injection flow rates of GLDA-flow in Run 3 are presented in Fig. 11, which indicated continuous permeability enhancement; particularly, permeability enhancement factor of c.a. 2.2 was achieved within 5 h, similar to those in Runs 1 and 2. Post-experimental X-ray CT sections (Fig. 8c) revealed that biotite dissolution was negligible, and the permeability enhancement was primarily due to fracture widening. The estimated post-experimentation porosity was 0.0057%, which was one order of magnitude lower than those in Runs 1 and 2. The concentrations of elements in the effluent, except for Si and Ca, were generally lower than those in Runs 1 and 2 (Fig. 9). Based on Takahashi et al. (2023), the effluent characteristics in Run 3 suggested enhanced quartz dissolution and a lower dissolution rate (compared to those at pH 4) of biotite and other minerals, which is consistent with the X-ray CT sections.

These results were consistent with the negligible axial shortening rates and low-energy AE activities in all experimental runs; the GLDA solutions might have effectively penetrated a certain number of wide fractures in the CFNs or penetrated in limited locations within the rock, such that the pressure and mineral dissolutions did not promote significant stress changes and deformation in the rock. These results suggested that the variation in differential stress does not significantly influence the permeability enhancement process in CFNs via GLDA solution injections under both weakly acidic and alkaline conditions.

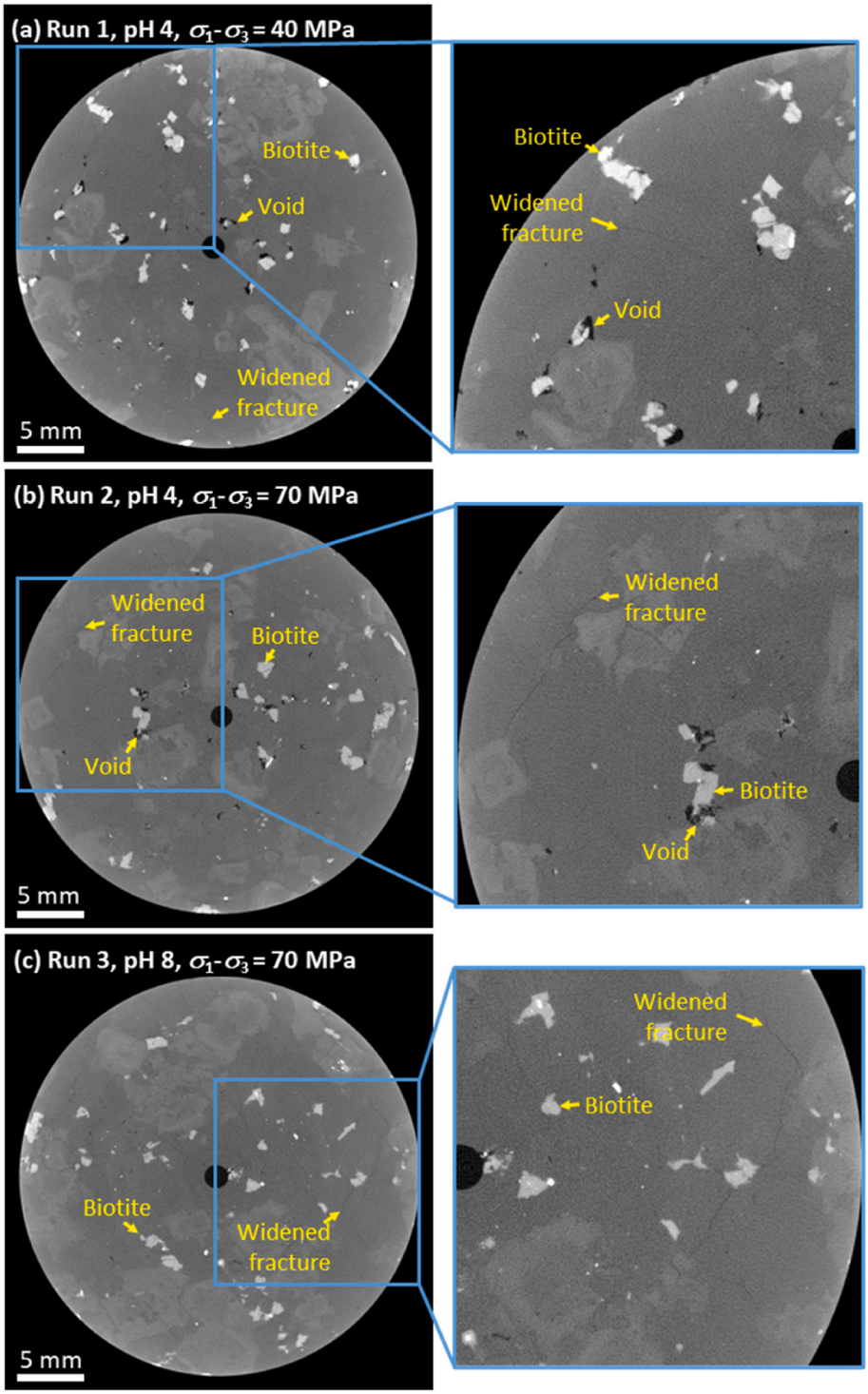

Fig. 8. X-ray CT images of the rock samples after the GLDA flow-through experiment at (a) pH 4 and differential stress = 40 MPa, (b) pH 4 and differential stress = 70 MPa, and (c) pH 8 and differential stress = 70 MPa. Yellow arrows show examples of biotite, voids, and widened fractures.

3.2. Permeability enhancement on a large scale and radial flow condition

Continuous sample shrinkage occurred throughout the experiment in Run 4. Nevertheless, the rock deformation rate (in the order of 10^{-1} μm·min^{-1}) and AE activity (sparse; energy in the order of 10^0–10^2 arb unit) during GLDA flow-through were mostly insignificant compared to those (deformation in the order of 10^0–10^1 μm·min^{-1}; AE energy in the order of 10^2 arb unit) in CO_2 fracturing (Pramudyo et al., 2021) at 300 °C under true-triaxial stress with 35-MPa differential stress conditions. Considerable AE activity occurred only during the increase in the borehole pressure owing to the change from water to GLDA injection. This was likely induced by the deformation of some fractures due to pore pressure changes around the borehole.

The time evolution of the differential pressure between the borehole and sample side faces, concentration of the elements in the effluent, and pH of the effluent are summarized in Fig. 12. The initial average permeability of the sample, computed during water injection when both injection and production pressures stabilized (time *T1*, Fig. 12a), was

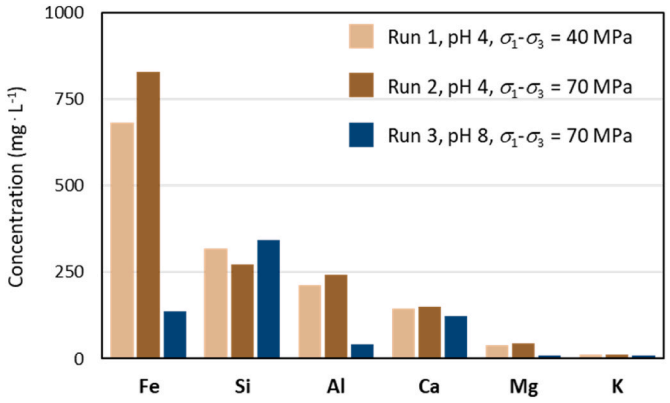

Fig. 9. Concentration of Fe, Si, Al, Ca, Mg, and K in the effluent from GLDA flow-through experiment in Run 1 (light brown), Run 2 (brown), and Run 3 (blue).

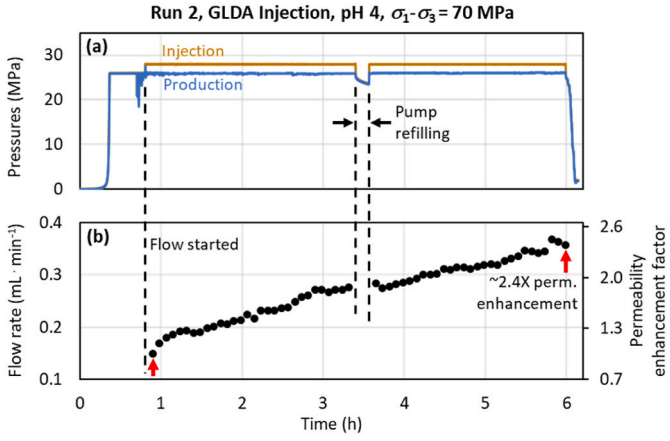

Fig. 10. (a) Injection and production pressures, and (b) calculated injection flow-rates and the corresponding permeability enhancement factor during GLDA flow-through in Run 2. Final permeability enhancement factor was obtained based on flow rate values pointed by red arrows.

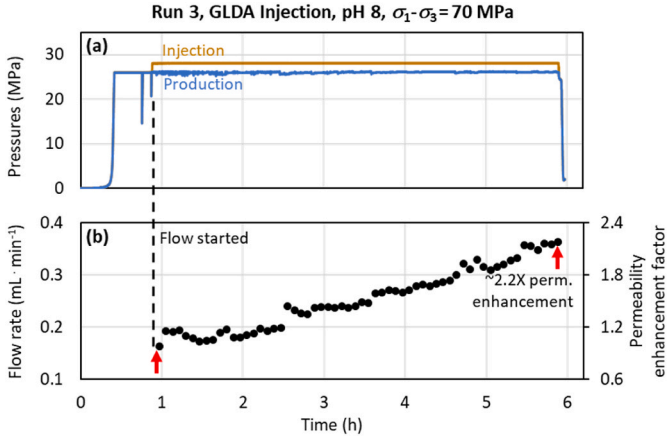

Fig. 11. (a) Injection and production pressures, and (b) calculated injection flow-rates and the corresponding permeability enhancement factor during GLDA flow-through in Run 3. Final permeability enhancement factor was obtained based on the flow rate values pointed by red arrows.

1.2×10^{-17} m^2. An increase in the differential pressure to approximately 2 MPa occurred within approximately 20 min of injecting the GLDA solution at pH 4 (time *T2*). This was because the GLDA solution had a

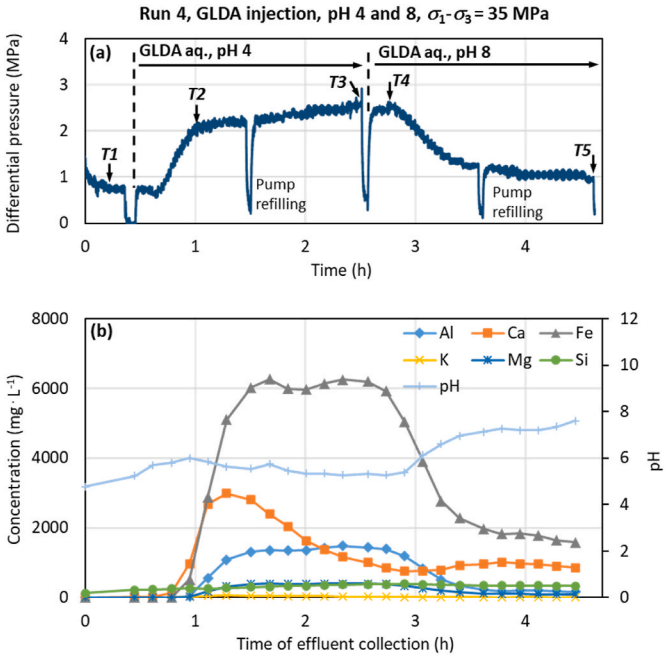

Fig. 12. Time evolution of (a) differential pressure between borehole and sample side faces, and (b) elemental concentrations in the effluent, as well as the pH during the GLDA-solution injections with the successive use of pH 4 and 8 under a true-triaxial stress condition (Run 4).

higher viscosity than water. Computed average permeability at time *T2* was 9.2×10^{-18} m^2, which was slightly lower than that at time *T1*. The lower computed permeability at time *T2* was likely due to fracture closure, as the pore pressure near the borehole decreased during the switch from water to GLDA solution injection. This also might be because most fractures did not effectively contribute to the flow of the GLDA solution. An increase in the concentration of elements in the effluent was then observed; a remarkable increase in Fe indicated biotite dissolution, whereas significant increases in Ca and Al indicated the dissolution of feldspar minerals.

After time *T2*, the differential pressure did not decrease, as expected from the permeability enhancement based on Eq. (4). At time *T3*, the computed average permeability was 7.2×10^{-18} m^2. Nonetheless, the elemental concentrations in the effluent, especially those of Fe and Al, remained high throughout the injection at pH 4, indicating that the dissolution of biotite and feldspar minerals continued. This characteristic was unlikely due to silica precipitation because the Si concentration in the effluent was generally between the solubility value of quartz (100 mg·L^{-1}) and amorphous silica (400 mg·L^{-1}) in water at 200 °C and 5 MPa (Manning, 1994; Karásek et al., 2013). Additionally, this phenomenon was also unlikely caused by suppressed mineral dissolution due to lack of GLDA concentration. Based on Al, Ca, Fe, and Mg concentrations, the computed concentration of unreacted GLDA-Na_4 in the effluents was > c.a. 62% of that (c.a. 0.65 mol·L^{-1}) in the initial 20 wt% GLDA-Na_4 solutions throughout the experiment.

We hypothesize that the minor rise in differential pressure during GLDA injection at pH 4 occurred because the high-viscosity GLDA solution penetrated more fractures, especially around the borehole, owing to the inferred higher pore pressure than that near the sample side faces. This speculation based on the tendency of higher incidence of void formation in zones with higher inferred pore pressure, such as near the injection side, compared to zones with lower inferred pore pressure during experiments. This tendency is observed in results reported by Takahashi et al. (2023), as well as in results presented in section 3.1 of our study. This presumably resulted in a higher permeability enhancement factor near the borehole than near the sample side faces.

Conversely, GLDA penetration should have occurred in fewer fractures near the side faces of the sample. Moreover, as suggested by Pramudyo et al. (2021), wider fractures in the CFN were more common in quartz than in feldspar minerals (Fig. 13a). Thus, mineral dissolution probably occurred in even fewer fractures near the sample side faces (Fig. 13b). If the injection at pH 4 was maintained for a longer time, a differential pressure drop might eventually be observed owing to the expansion of the zone with higher permeability enhancement.

At time *T4* (immediately after the start of GLDA injection at pH 8), the average permeability was 7×10^{-18} m^2, which was similar to that at time *T3*. However, a differential pressure drop was observed after *T4*. Enhanced quartz dissolution (Takahashi et al., 2023), wherein wider fractures are more common in granite CFN, likely provided a considerable number of enhanced flow-paths. Together with the chemically stimulated fractures in the feldspar minerals, the chemically stimulated fractures in quartz presumably created more and enhanced connecting flow paths between the borehole and the sample-side faces (Fig. 13c). As the differential pressure decreased, the pore pressure in the sample likely also decreased; the penetration of GLDA into more fractures became less likely. Therefore, the permeability enhancement rate became slower, as reflected by the slower decrease in the differential pressure (Fig. 12a) towards the end of the experiment. At the end of the injection at pH 8 (time *T5*), an average permeability of 1.8×10^{-17} m^2 was obtained, and it was approximately 1.6-times higher than the initial average permeability.

Assuming that the radius of the intense mineral dissolution (higher permeability enhancement) zone was 2 cm from the center (i.e., r_1, based on radius of the borehole plus radius of the samples used at conventional-triaxial stress conditions), and assuming that permeability enhancement near sample side faces was negligible, the permeability around the borehole at time *T5* should have been approximately 2.9×10^{-17} m^2 or 2.5-times the initial value [Eq. (5)]. This implied that the GLDA solution injection at each pH contributed to an approximately 1.57-permeability enhancement factor (i.e., the square root of the 2.5-enhancement factor) near the borehole. The c.a. 1.57-permeability enhancement factor for each pH condition was comparable to that obtained from experiments under conventional triaxial stress conditions, considering the shorter injection duration (2 h) for the pH condition in this experiment versus 5 h in the experiment performed under conventional triaxial stress conditions.

The P-wave velocities in the sample increased compared to those before the experiment (Table 2, Fig. 14), which was due to a decrease in the apertures of the thermally induced fractures (formed at atmospheric pressure) when the sample was subjected to compression (Watanabe et al., 2021b; Salalá et al., 2023; Takahashi et al., 2023). If the P-wave velocity measurements (before and after GLDA solution injection) were performed while the sample was under stressed conditions, void formation and fracture widening due to mineral dissolution would result in a certain degree of P-wave velocity reduction. Nonetheless, the measured average P-wave velocities of the sample post-experimentation were isotropic (Table 2), which suggested no preferential orientation of wide fractures (Hsu and Schoenberg, 1993), and was thus, isotropic permeability. However, the P-wave velocity distribution did not demonstrate a clear distribution of zones with a higher number of voids with respect to borehole position.

The X-ray CT sections of the cores obtained from the samples verified that there were more voids near the borehole than near the sample side

Table 2
Average P-wave velocities in each stress direction before and after Experimental run 4.

Direction	Average P-wave velocities (m·s^{-1})			
	Before experiment		After experiment	
	Value	% of value at σ_1 direction	Value	% of value at σ_1 direction
σ_1	1819.6	100.0	2402.3	100.0
σ_2	1651.4	90.8	2578.1	107.3
σ_3	2048.5	112.6	2241.6	93.3

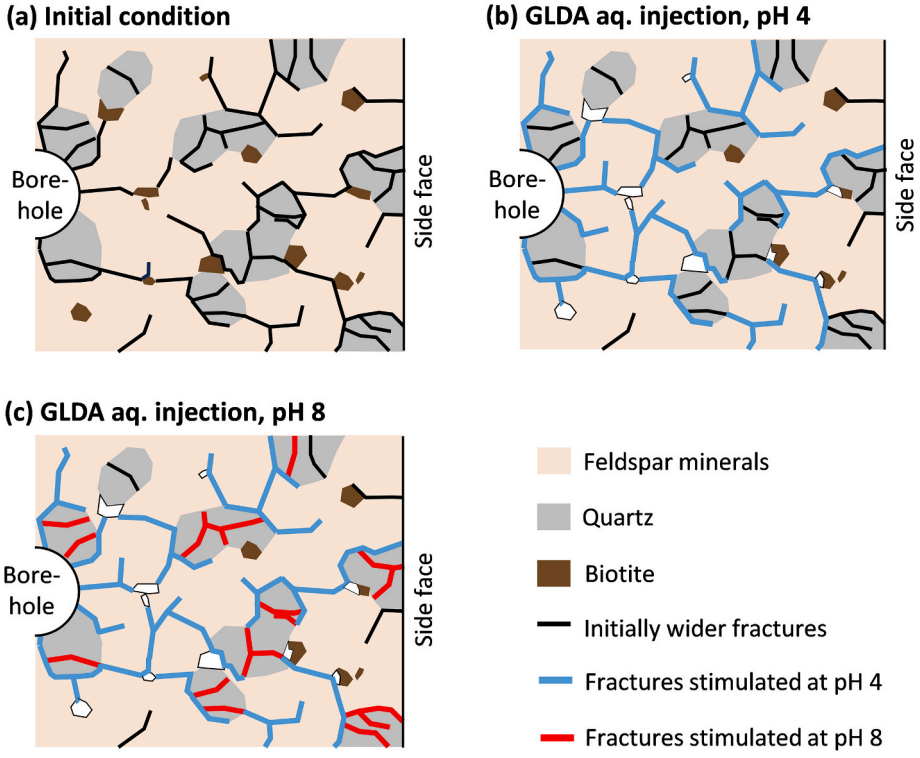

Fig. 13. Illustration (not to scale) of permeability enhancement on the sample due to successive injection of GLDA solutions at pH 4 and 8 under radial flow condition in Run 4. (a) initial condition, (b) during GLDA aq. injection at pH 4, and (c) during GLDA aq. injection at pH 8.

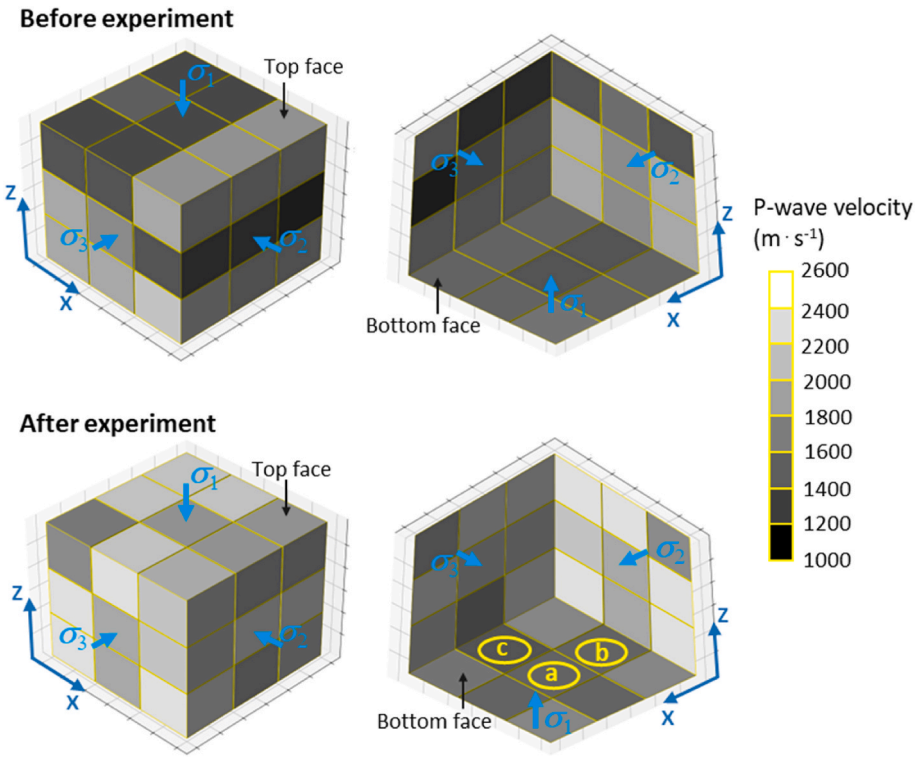

Fig. 14. Distribution of estimated P-wave velocities for the sample before and after the chelating agent-injection experiment of Run 4. Left and right cubes show each other's invisible faces. Yellow circles in the bottom face of the after-experiment cube show the location of cores obtained for X-ray CT scan; (a) around borehole, (b) at centered σ_1–σ_2 plane, and (c) at centered σ_1–σ_3 plane.

faces (Fig. 15). There were also approximately 55%-more visible fractures near the borehole than near the sample side faces; these fractures should have been chemically stimulated by the GLDA solutions. These observations agree with the computed porosity, which was approximately 0.11% around the borehole and 0.028% near the sample side faces. Nevertheless, the X-ray CT images suggested that there was no relationship between the stress orientation and the distribution of voids and visible fractures.

3.3. Practical implication for field chelating agent injection

The present experiments suggested that because of the high viscosity of the GLDA solution, mineral dissolution occurs effectively only in a certain number of wide fractures or in limited locations in the rock, so as not to promote significant rock deformation. Therefore, the GLDA solution can be injected into the CFN at pressures close to σ_3, even if the pressure is higher than $P_{p,frac}$, to allow efficient penetration into the fracture network. Nonetheless, in naturally fractured geothermal environments, the GLDA solution may be injected below the pressure required for hydroshearing to minimize excessive induced seismicity; however, this requires further investigation. Because the pressure gradient decreases in the chemically stimulated volume, a constant injection pressure allows for an optimum chemical stimulation radius based on Eq. (5). The pore-pressure values in the chemically-stimulated zone will be close to injection pressure value; thus, pressure gradient in the stimulation front will be sufficiently high to maintain the GLDA flow into the chemically unstimulated volume and enable the expansion of the stimulated radius (which can be expressed by r_1 in Eq. (5)).

Owing to the tendency of higher permeability enhancement near the injection borehole than far from the borehole in the GLDA solution injection at pH 4, low GLDA concentrations may be injected to reduce the solution viscosity. This allows penetration into more fractures and achieves a larger chemically stimulated volume than when the solution is more concentrated. Lower concentrations would also reduce mineral dissolution rates, which are beneficial for achieving a larger chemically stimulated volume with more even permeability enhancement (Rose et al., 2010; Watanabe et al., 2021b). Although more fractures would be penetrated while injecting low-concentration GLDA solution, excessive deformations and acoustic emissions are still less likely when a fluid that is more viscous than water is injected. This is based on the relatively slow slip induced by water injection on a granite sawcut, compared to those induced by CO_2 injection (Pramudyo et al., 2023). Subsequent GLDA solution injection at pH 8 should also be conducted using low-concentration GLDA to achieve penetration into numerous fractures and enable a large chemical stimulation radius. Future experiments involving GLDA injection on large scale samples could be essential to better understand the expansion of stimulated zones. These studies should consider the impact of varying GLDA concentrations and geothermal temperature, which may influence the reaction rate.

3.4. Creating geothermal reservoir using CO_2 injection and additional methods

Chabora et al. (2012) described a scheme for well stimulation in a conventional geothermal environment (depth and temperature of c.a. 1 km and 190 °C) predominantly using water injection. In principle, the scheme consists of phases, such as hydroshearing, chemical stimulation, and controlled hydraulic fracturing, which generally progress from phases incorporating low pressure to phases with high pressure. Each phase also comprises repeats from low to high pressures. The decision to repeat a stimulation method using high pressures in a phase, or proceeding to the next phases, was based on whether the economic water injectivity (which reflects permeability) of $\geq$0.75 gpm·psi^{-1} (gallon per minute per pound per square inch) had been achieved.

A general scheme similar to that described by Chabora et al. (2012) may be employed in CO_2 injection into conventional geothermal environment of approximately 150–200 °C; CO_2 fracturing (i.e., achieving CFN using CO_2 injection) or hydroshearing using CO_2 in case of

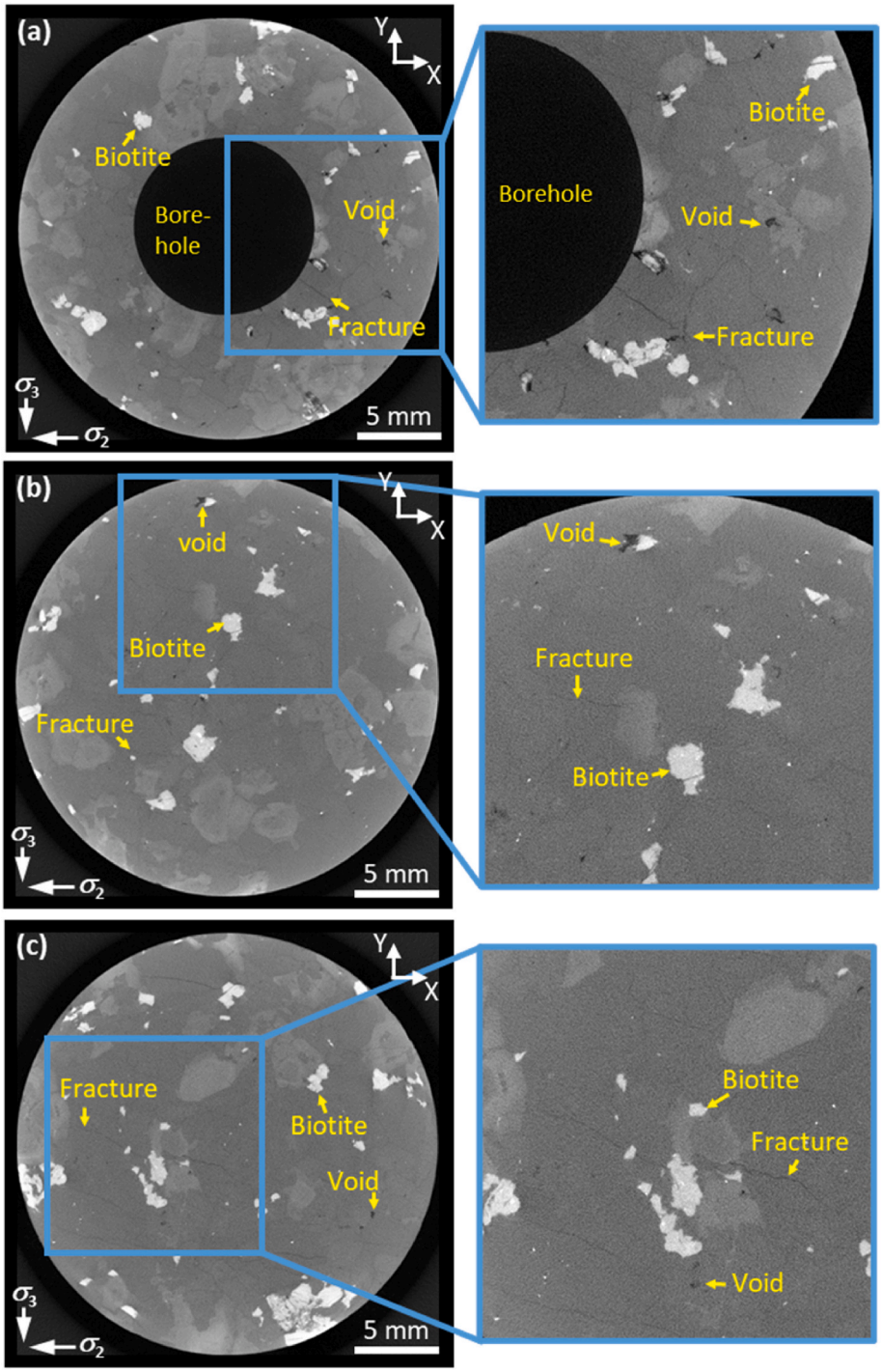

Fig. 15. Representative X-ray CT images of the rock sample at σ_2–σ_3 planes after injecting GLDA solutions in Run 4: (a) around borehole, (b) near sample side face at centered σ_1–σ_2 plane, and (c) near sample side face at centered σ_1–σ_3 plane. Yellow arrows pointing the example of biotite crystals, voids, and fractures.

naturally fractured environment should be performed to create or recreate a complex network of permeable fractures (Fig. 16). Hydraulic stimulation allows deep penetration of aqueous GLDA solutions in the later phase if the preceding hydraulic stimulation does not achieve economic injectivity. If economic injectivity is not achieved after GLDA injection into the hydrosheared natural fracture network, CO_2 fracturing may be performed, followed by another GLDA injection, as necessary. CO_2 fracturing in naturally fractured environments is achieved by increasing the CO_2 pressure to $P_{p,frac}$, which is always higher (governed by the Griffith failure criterion of rock matrix) than the pressure required for the shearing of natural fractures (controlled by the Coulomb failure criterion of natural fractures) for the same stress state and rock tensile strength (Pramudyo et al., 2023). Finally, to enhance injectivity or expand the fractured zone through flow-induced microfracturing (Goto et al., 2021), long-duration pressurization at or above the fracture-formation pressure ($P_{p,frac}$) can be carefully implemented after CO_2 fracturing and GLDA injection. This approach must be cautiously managed to avoid inducing excessive seismic activity. Note that the threshold for economic injectivity in CO_2-based EGS differs from the generally accepted value in water-based EGS. This is because CO_2 has a lower specific heat capacity than water, but its low-viscosity allows for a higher mass flow rate (Brown, 2000; Pruess, 2006). Thus, the threshold

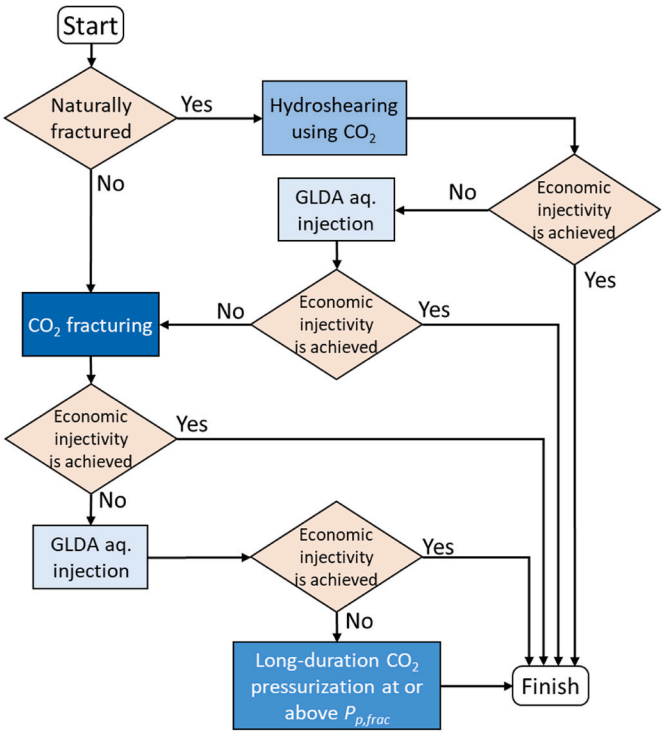

Fig. 16. General schemes for creating reservoirs in geothermal environments of approximately 150–200 °C.

for economic injectivity in CO_2-based EGS requires further comprehensive investigation.

Chelating agents, including GLDA, generally degrade relatively fast above 200 °C (Martell et al., 1975; Sokhanvarian et al., 2016). This characteristic makes GLDA solution injection difficult to be implemented in geothermal environment with temperatures >200 °C (including superhot geothermal environments). Thus, creating geothermal reservoir at temperatures of >200 °C may be performed in phases, as depicted by Fig. 17. CO_2 fracturing, or hydroshearing using CO_2 in case of naturally fractured environment, should be performed

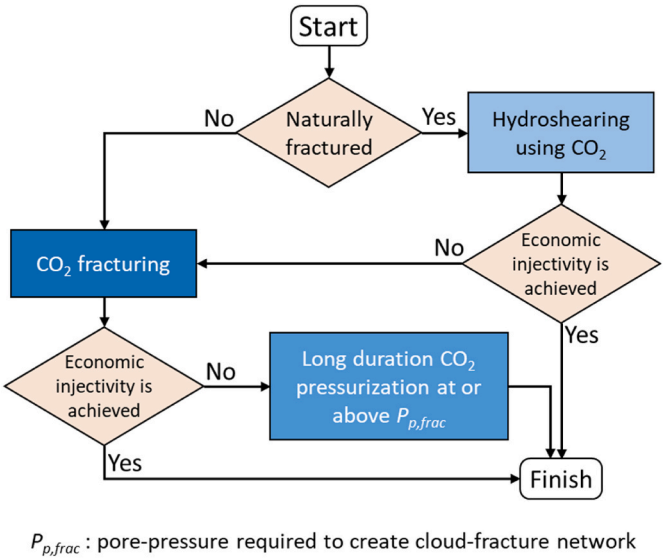

Fig. 17. General schemes for creating reservoirs in geothermal environments with temperatures of > c.a. 200 °C.

first. If economic injectivity is not achieved during the initial hydroshearing, CO_2 fracturing should be performed later by increasing the CO_2 pressure to $P_{p,frac}$. Long-duration CO_2 pressurization at or above $P_{p,frac}$ may also be performed, with care to minimize the risk of large induced seismicity, if economic injectivity is still not achieved after CO_2 fracturing, or if expansion of the fractured zone is intended (Goto et al., 2021).

Therefore, creating a granitic geothermal reservoir using CO_2 injection along with additional stimulation methods appears to be feasible. Nevertheless, several aspects must be addressed before their application on a field scale. First, because CO_2 has a lower viscosity than water, the stimulation processes and growth of the stimulated zone during CO_2 injection probably differ from those known for water injections. Second, the thermal extraction characteristics of CO_2 injection-induced stimulated natural fractures and CFN are yet to be elucidated. Third, CO_2 may dissolve in the resident brine in the stimulation front, where mineral dissolution or deposition may occur (Ueda et al., 2005) and affect reservoir growth. Fourth, the process of permeability enhancement at the reservoir scale while injecting chelating agent solutions must be elucidated. Fifth, the significance of geological complexity, such as the spatial variation in rock types and geological structures, remains unclear. Understanding these aspects is essential, for instance, to determine the volumes required and the details of the injection strategies for CO_2 injection and additional methods. In such cases, newly designed laboratory experiments and computer simulations may be suitable to elucidate these points.

4. Conclusion

In this study, we experimentally elucidated that the injection of a GLDA solution into CO_2 injection-induced CFNs results in a similar permeability enhancement factor under a conventional geothermal temperature with varying stress states, under both weakly acidic and alkaline conditions, within the same injection duration. The high viscosities of the GLDA solutions likely caused GLDA penetration, and mineral dissolution effectively occurred only in some wide fractures. Thus, significant deformation in the fracture network was not promoted. In contrast, fracture deformation was more likely to occur during CO_2 injection.

At a large scale and in a radial flow geometry, GLDA solution injection at pH 4 (weakly acidic conditions) resulted in a zone with a high inferred permeability enhancement factor around the borehole. This was attributed to the more intense void formation (due to biotite dissolution) and fracture aperture widening (due to the dissolution of mainly feldspar minerals) near the borehole, owing to the higher inferred pore pressure, than those far from the borehole. This suggested that weakly acidic GLDA solutions should be injected at low concentrations to reduce the viscosity and dissolution rate, thus, achieving GLDA penetration into more fractures and a greater chemically stimulated radius. A constant injection pressure would also achieve an optimum chemical stimulation radius because it would maintain a large pressure gradient in the stimulation front, enhancing the flow of the GLDA solution into the chemically unstimulated zone. Subsequent injection at pH 8 should also be performed using a low GLDA concentration and constant injection pressure, such that the solution at pH 8 can reach most parts of the zone previously stimulated at pH 4.

Based on the findings of this study, combined with knowledge from previous studies, two general stimulation schemes can be created. Both schemes suggest risk reduction of large-magnitude induced seismicity, where the stimulation should be generally initiated using a method that requires the lowest pressure. In conventional geothermal environments with temperatures up to 200 °C, CO_2 should be initially injected to achieve the initial permeability enhancement through hydroshearing or CFN formation. The next phase of chemical stimulation using a chelating agent and further hydraulic stimulations, including long duration CO_2-pressurization at or above fracture pressure, can be performed based on

whether commercial injectivity has been achieved. In geothermal environments with temperatures > c.a. 200 °C, the scheme would comprise CO_2 injection to achieve CFN or hydroshearing and further stimulation by long CO_2-pressurization duration at or above fracture pressure, if necessary.

Overall, the present study provides insights on the preferable stimulation strategies for creating geothermal reservoirs using CO_2 injection and additional methods. Nevertheless, before their application in field scale, further comprehensive studies are necessary to address unclear points, such as the growth of the stimulated zones, interactions with resident brine, and the significance of geological complexity.

Declaration of generative artificial intelligence (AI) in scientific writing

Generative AI was not used in writing the manuscript of this study.

CRediT authorship contribution statement

Eko Pramudyo: Conceptualization, Data curation, Formal analysis, Investigation, Methodology, Visualization, Writing - original draft. **Luis Salalá:** Conceptualization, Formal analysis, Investigation, Methodology, Visualization, Writing - original draft. **Ryota Goto:** Formal analysis, Investigation, Methodology, Writing - review & editing. **Jiajie Wang:** Formal analysis, Investigation, Writing - review & editing. **Kazumasa Sueyoshi:** Formal analysis, Investigation, Writing - review & editing. **Lena Muhl:** Investigation, Writing - review & editing. **Kiyotoshi Sakaguchi:** Funding acquisition, Methodology, Resources, Validation, Writing - review & editing. **Noriaki Watanabe:** Conceptualization, Funding acquisition, Methodology, Project administration, Supervision, Validation, Writing - review & editing.

Declaration of competing interest

The authors declare the following financial interests/personal relationships which may be considered as potential competing interests: Noriaki Watanabe reports financial support was provided by Japan Society for the Promotion of Science. Ryota Goto reports financial support was provided by Japan Society for the Promotion of Science. Jiajie Wang reports financial support was provided by Japan Society for the Promotion of Science. Noriaki Watanabe reports financial support was provided by Japan Science and Technology Agency. Noriaki Watanabe reports financial support was provided by Japan International Cooperation Agency. Noriaki Watanabe reports that Tohoku University holds Japan Patent #7115692 in relation to chelating-agent-based chemical stimulation.

Data availability

Data will be made available on request.

Acknowledgements

This study was partially supported by the Japan Society for the Promotion of Science (JSPS) through Grants-in-Aid for Scientific Research (S) (No. 22H04932), Scientific Research (B) (No. 22H02015 and 23H01903), Challenging Research (Pioneering) (No. 21K18200), JSPS Early-Career Scientist (No. 21K14571), and JSPS Fellows (No. 20J20108). This study was supported by the Japan Science and Technology Agency (JST) and the Japan International Cooperation Agency (JICA) through the JST/JICA Science and Technology Research Partnership for Sustainable Development program (No. JPMJSA1703). The authors would like to thank Toei Scientific Industrial Co., Ltd. for manufacturing the experimental system.

References

Brown, D.W., 2000. A hot dry rock geothermal energy concept utilizing supercritical CO_2 instead of water. Proceedings of the Twenty-fifth Workshop on Geothermal Reservoir Engineering 233–238.

Cao, M., Sharma, M.M., 2023. Effect of fracture geometry, topology and connectivity on energy recovery from enhanced geothermal systems. Energy 282, 128368. https://doi.org/10.1016/j.energy.2023.128368.

Chabora, E., Zemach, E., Spielman, P., Drakos, P., Hickman, S., Lutz, S., Boyle, K., Falconer, A., Robertson-Tait, A., Davatzes, N.C., Rose, P., Majer, E., Jarpe, S., 2012. Hydraulic stimulation of well 27-15, Desert Peak geothermal field, Nevada, USA. In: Proceedings of Thirty-Seventh Workshop on Geothermal Reservoir Engineering, vol. 30. Stanford University, Stanford.

Cox, S.F., 2010. The application of failure mode diagrams for exploring the roles of fluid pressure and stress states in controlling styles of fracture-controlled permeability enhancement in faults and shear zones. Geofluids 10 (1–2), 217–233. https://doi.org/10.1111/j.1468-8123.2010.00281.x.

Dake, L.P., 1983. Fundamentals of Reservoir Engineering. Elsevier, Amsterdam, the Netherlands.

Gandossi, L., Estorff, U.V., 2015. An Overview of Hydraulic Fracturing and Other Formation Stimulation Technologies for Shale Gas Production – Update 2015. EUR 26347. Publications Office of the European Union, Luxembourg (Luxembourg). https://doi.org/10.2790/379646. JRC98582.

Gautam, P.K., Verma, A.K., Jha, M.K., Sharma, P., Singh, T.N., 2018. Effect of high temperature on physical and mechanical properties of Jalore granite. J. Appl. Geophys. 159, 460–474. https://doi.org/10.1016/j.jappgeo.2018.07.018.

Goto, R., Nakayama, D., Takahashi, R., Pramudyo, E., Takuma, K., Watanabe, N., 2023. Cooling-induced permeability enhancement for networks of microfractures in superhot geothermal environments. Geoth. Energy 11 (1), 7. https://doi.org/10.1186/s40517-023-00251-9.

Goto, R., Watanabe, N., Sakaguchi, K., Miura, T., Chen, Y., Ishibashi, T., Pramudyo, E., Parisio, F., Yoshioka, K., Nakamura, K., Komai, T., Tsuchiya, N., 2021. Creating cloud-fracture network by flow-induced microfracturing in superhot geothermal environments. Rock Mech. Rock Eng. 54, 2959–2974. https://doi.org/10.1007/s00603-021-02416-z.

Griffith, A.A., 1924. Theory of Rupture. First International Congress on Applied Mechanics, pp. 56–63.

Heidaryan, E., Hatami, T., Rahimi, M., Moghadasi, J., 2011. Viscosity of pure carbon dioxide at supercritical region: measurement and correlation approach. J. Supercrit. Fluids 56 (2), 144–151. https://doi.org/10.1016/j.supflu.2010.12.006.

Hsu, C.-J., Schoenberg, M., 1993. Elastic waves through a simulated fractured medium. Geophysics 58 (7), 964–977. https://doi.org/10.1190/1.1443487.

Isaka, B.A., Ranjith, P.G., Rathnaweera, T.D., Wanniarachchi, W.M., Kumari, W.G., Haque, A., 2019. Testing the frackability of granite using supercritical carbon dioxide: insights into geothermal energy systems. J. CO_2 Util. 34, 180–197. https://doi.org/10.1016/j.jcou.2019.06.009.

Ishida, T., Chen, Y., Bennour, Z., Yamashita, H., Inui, S., Nagaya, Y., Naoi, M., Chen, Q., Nakayama, Y., Nagano, Y., 2016. Features of CO_2 fracturing deduced from acoustic emission and microscopy in laboratory experiments. J. Geophys. Res. Solid Earth 121 (11), 8080–8090. https://doi.org/10.1002/2016JB013365.

Ishihara, S., 1991. Aji stone: the historical and modern use, and its geologic background. Chishitsu News 441, 60–67 (in Japanese).

Jaeger, J.C., Cook, N.G., Zimmerman, R., 2007. Fundamental of Rock Mechanics, 4 ed. John Wiley and Sons.

Karásek, P., Šťavíková, L., Planeta, J., Hohnová, B., Roth, M., 2013. Solubility of fused silica in sub-and supercritical water: estimation from a thermodynamic model. J. Supercrit. Fluids 83, 72–77. https://doi.org/10.1016/j.supflu.2013.08.012.

Kwiatek, G., Saarno, T., Ader, T., Bluemle, F., Bohnhoff, M., Chendorain, M., Dresen, G., Heikkinen, P., Kukkonen, I., Leary, P., Leonhardt, M., Malin, P., Martínez-Garzón, P., Passmore, K., Passmore, P., Valenzuela, S., Wollin, C., 2019. Controlling fluid-induced seismicity during a 6.1-km-deep geothermal stimulation in Finland. Sci. Adv. 5 (5), eaav7224. https://doi.org/10.1126/sciadv.aav7224.

Lin, W., Nakamura, T., Takahashi, M., 2003. Anisotropy of thermal property, ultrasonic wave velocity, strength property and deformability in Inada granite. J. Japan Soc. Engi. Geol. 44 (3), 175–187(in Japanese). doi:10.5110/jjseg.44.175.

Manning, C.E., 1994. The solubility of quartz in H_2O in the lower crust and upper mantle. Geochem. Cosmochim. Acta 58 (22), 4831–4839. https://doi.org/10.1016/0016-7037(94)90214-3.

Martell, A.E., Motekaitis, R.J., Fried, A.R., Wilson, J.S., MacMillan, D.T., 1975. Thermal decomposition of EDTA, NTA, and nitrilotrimethylenephosphonic acid in aqueous solution. Can. J. Chem. 53 (22), 3471–3476. https://doi.org/10.1139/v75-498.

Moridis, G., 2018. Literature Review and Analysis of Waterless Fracturing Methods. Lawrence Berkeley National Laboratory.

Pramudyo, E., Goto, R., Sakaguchi, K., Nakamura, K., Watanabe, N., 2023. CO_2 injection-induced shearing and fracturing in naturally fractured conventional and superhot geothermal environments. Rock Mech. Rock Eng. 56 (3), 1663–1677. https://doi.org/10.1007/s00603-022-03153-7.

Pramudyo, E., Goto, R., Watanabe, N., Sakaguchi, K., Nakamura, K., Komai, T., 2021. CO_2 injection-induced complex cloud-fracture networks in granite at conventional and superhot geothermal conditions. Geothermics 97, 102265. https://doi.org/10.1016/j.geothermics.2021.102265.

Pruess, K., 2006. Enhanced geothermal systems (EGS) using CO_2 as working fluid—a novel approach for generating renewable energy with simultaneous sequestration of carbon. Geothermics 35 (4), 351–367. https://doi.org/10.1016/j.geothermics.2006.08.002.

Rose, P.E., Xu, T., Fayer, S., Pruess, K., 2010. Chemical Stimulation for EGS: the Use of Chelating Agents at High pH for the Simultaneous Dissolution of Calcium Carbonate, Silicas, and Silicates. Proceedings World Geothermal Congress, Bali, Indonesia.

Rutqvist, J., Rinaldi, A.P., 2019. Fault Reactivation and Seismicity Associated with Geologic Carbon Storage, Shale-Gas Fracturing and Geothermal Stimulation–Observations from Recent Modeling Studies. 14th ISRM Congress, OnePetro.

Salalá, L., Takahashi, R., Argueta, J., Wang, J., Watanabe, N., Tsuchiya, N., 2023. Permeability enhancement and void formation by chelating agent in volcanic rocks (Ahuachapán and Berlín geothermal fields, El Salvador). Geothermics 107. https://doi.org/10.1016/j.geothermics.2022.102586.

Sasada, M., 1991. Inada granite. Chishitsu News 441, 34–40 (in Japanese).

Secor, D.T., 1965. Role of fluid pressure in jointing. Am. J. Sci. 263 (8), 633–646. https://doi.org/10.2475/ajs.263.8.633.

Sokhanvarian, K., Nasr-El-Din, H.A., de Wolf, C.A., 2016. Thermal stability of oilfield aminopolycarboxylic acids/salts. SPE Prod. Oper. 31 (1), 12–21. https://doi.org/10.2118/157426-PA.

Takahashi, R., Wang, J., Watanabe, N., 2023. Process and optimum pH for permeability enhancement of fractured granite through selective mineral dissolution by chelating agent flooding. Geothermics 109, 102646. https://doi.org/10.1016/j.geothermics.2022.102646.

Takahashi, Y., Miyazaki, K., Nishioka, Y., 2011. Plutonic rocks and metamorphic rocks in the Tsukuba Mountains. J. Geol. Soc. Jpn. 117, 21–31. https://doi.org/10.5575/geosoc.117.S21 (in Japanese).

Takaya, Y., 2011. Experimental study on alteration characteristics during chemical weathering of granite. Geogr. Rev. Jpn. Ser. A. 84, 131–144. https://doi.org/10.4157/grj.84.131 (in Japanese with English abstract).

Tester, J.W., Anderson, B.J., Batchelor, A.S., Blackwell, D.D., DiPippo, R., Drake, E.M., Garnish, J., Livesay, B., Moore, M.C., Nichols, K., Petty, S., Toksöz, M.N., Veatch Jr., R.W., 2006. Impact of Enhanced Geothermal Systems (EGS) on the united states in the 21st Century. Idaho National Laboratory, Renewable Energy and Power Department. Massachusetts Institute of Technology. Retrieved from. https://energy.mit.edu/wp-content/uploads/2006/11/MITEI-The-Future-of-Geothermal-Energy.pdf.

Ueda, A., Kato, K., Ohsumi, T., Yajima, T., Ito, H., Kaieda, H., Metcalfe, R., Takase, H., 2005. Experimental studies of CO_2-rock interaction at elevated temperatures under hydrothermal conditions. Geochem. J. 39 (5), 417–425.

Wang, J., Watanabe, N., Inomoto, K., Kamitakahara, M., Nakamura, K., Komai, T., Tsuchiya, N., 2022. Sustainable process for enhanced CO_2 mineralization of calcium silicates using a recyclable chelating agent under alkaline conditions. J. Environ. Chem. Eng. 10 (1), 107055 https://doi.org/10.1016/j.jece.2021.107055.

Watanabe, N., Egawa, M., Sakaguchi, K., Ishibashi, T., Tsuchiya, N., 2017b. Hydraulic fracturing and permeability enhancement in granite from subcritical/brittle to supercritical/ductile conditions. Geophys. Res. Lett. 44 (11), 5468–5475. https://doi.org/10.1002/2017GL073898.

Watanabe, N., Numakura, T., Sakaguchi, K., Saishu, H., Okamoto, A., Ingebritsen, S.E., Tsuchiya, N., 2017a. Potentially exploitable supercritical geothermal resources in the ductile crust. Nat. Geosci. 10, 140–144. https://doi.org/10.1038/ngeo2879.

Watanabe, N., Abe, H., Okamoto, A., Nakamura, K., Komai, T., 2021a. Formation of amorphous silica nanoparticles and its impact on permeability of fractured granite in superhot geothermal environments. Sci. Rep. 11 (1) https://doi.org/10.1038/s41598-021-84744-2.

Watanabe, N., Saito, K., Okamoto, A., Nakamura, K., Ishibashi, T., Saishu, H., Komai, T., Tsuchiya, N., 2020. Stabilizing and enhancing permeability for sustainable and profitable energy extraction from superhot geothermal environments. Appl. Energy 260. https://doi.org/10.1016/j.apenergy.2019.114306.

Watanabe, N., Sakaguchi, K., Goto, R., Miura, T., Yamane, K., Ishibashi, T., Chen, Y., Komai, T., Tsuchiya, N., 2019. Cloud-fracture networks as a means of accessing superhot geothermal energy. Sci. Rep. 9 (1), 1–11. https://doi.org/10.1038/s41598-018-37634-z.

Watanabe, N., Takahashi, K., Takahashi, R., Nakamura, K., Kumano, Y., Akaku, K., Tamagawa, T., Komai, T., 2021b. Novel chemical stimulation for geothermal reservoirs by chelating agent driven selective mineral dissolution in fractured rocks. Sci. Rep. 11 (1), 19994 https://doi.org/10.1038/s41598-021-99511-6.

Wilkins, R., Menefee, A.H., Clarens, A.F., 2016. Environmental life cycle analysis of water and CO_2-based fracturing fluids used in unconventional gas production. Environ. Sci. Technol. 50 (23), 13134–13141. https://doi.org/10.1021/acs.est.6b02913.

Yamaguchi, U., 1970. The number of test-pieces required to determine the strength of rock. Int. J. Rock Mech. Min. Sci. Geomech. Abstr. 7 (2), 209–227. https://doi.org/10.1016/0148-9062(70)90013-6.

Yu, P., Dempsey, D., Archer, R., 2021. A three-dimensional coupled thermo-hydro-mechanical numerical model with partially bridging multi-stage contact fractures in horizontal-well enhanced geothermal system. Int. J. Rock Mech. Min. Sci. 143, 104787 https://doi.org/10.1016/j.ijrmms.2021.104787.